Check for updates

Angewandte Chemie

Angewandte Chemie

Zitierweise: *Angew. Chem. Int. Ed.* **2026**, e6084718
doi.org/10.1002/anie.6084718

FORSCHUNGSARTIKEL

Orbital Fine-Tuning of d/p-Band Centers Enables Highly Preferential Single-Electron Oxygen Activation

Zili Lin[1,2] | Yanli Wang[1] | Zhenjun Xiao[1] | Ping Chen[1] | Yishun Wang[3] | Lingzhi Shen[1] | Zheng Hu[1] | Zihong Xu[1] | Siling Zhang[1] | Linsheng Liu[1] | Zheng Fang[4] | Daguang Li[5] | Wenying Lv[1] | Guoguang Liu[1]

[1]Guangdong Key Laboratory of Environmental Catalysis and Health Risk Control, School of Environmental Science and Engineering, Institute of Environmental Health and Pollution Control, Guangdong University of Technology, Guangzhou, China | [2]School of Marine Science and Technology, Shanwei Institute of Technology, Shanwei, China | [3]School of Environment and Energy, Key Laboratory of Pollution Control and Ecosystem Restoration in Industry Clusters (Ministry of Education), South China University of Technology, Guangzhou, China | [4]State Key Laboratory of Geomicrobiology and Environmental Changes, China University of Geosciences, Wuhan, China | [5]College of Light Chemical Industry and Materials Engineering, Shunde Polytechnic University, Foshan, China

Correspondence: Ping Chen (gdutchp@163.com) | Wenying Lv (lvwy612@163.com)

Received: 22 December 2025 | **Revised:** 9 August 2026 | **Accepted:** 13 August 2026

Keywords: d/p-band center | photocatalytic | polymer phenylethynylcopper | reactive oxygen species | water decontamination

ABSTRACT

The single-electron photocatalytic reduction of molecular oxygen to superoxide radicals ($O_2^{\bullet-}$) represents the rate-determining step in environmental photochemistry, yet achieving high selectivity toward this pathway remains a formidable challenge. Here, we introduce a conceptually driven orbital-hybridization strategy to precisely regulate the d/p orbitals of polymeric phenylethynylcopper (PECu) through chlorine doping. Rather than acting as a conventional heteroatom dopant, Cl^- serves as an "orbital fine-tuner", enhancing the coordination polarization of C≡C—Cu units and shortening the Cu—Cu ladder spacing to construct an efficient metal–metal charge-transfer (MMCT) channel. This interfacial electronic engineering markedly improved d/p-band center proximity ($\Delta\varepsilon_{d\text{-}p}$), thereby optimizing the adsorption and activation of O_2 intermediates at alkyne active sites. The optimized PCC photocatalyst exhibits exceptional selectivity for the $O_2 \rightarrow O_2^{\bullet-}$ single-electron reduction pathway, achieving a superoxide yield of 471.38 μmol/L and significantly enhanced water decontamination performance. This work extends conventional band-center engineering from activity optimization to highly preferential single-electron oxygen activation by identifying d/p-band-center proximity as a key electronic descriptor governing selective single-electron O_2 reduction.

1 | Introduction

The photocatalytic activation of molecular oxygen to generate reactive oxygen species (ROS) is a fundamental process in sustainable water purification [1–3]. Among these reactions, the precise utilization of photogenerated electrons via a single-electron transfer pathway to produce superoxide radicals ($O_2^{\bullet-}$) is critical for the efficient conversion of light energy [4, 5]. In recent years, substantial progress has been achieved in promoting the separation of photogenerated charge carriers through strategies such as constructing heterojunctions [6], implementing defect engineering [7], and applying external fields [8]. However, a more fundamental yet often overlooked scientific issue is the catalyst's intrinsic electronic structure, particularly its ability to reduce O_2 using conduction band (CB) electrons. This property establishes both the prerequisite and the upper limit of the single-electron oxygen reduction process. Consequently, developing benchmark materials with highly negative CB potentials and efficient interfacial electron transfer capabilities is essential for overcoming current efficiency bottlenecks.

All rights reserved, including rights for text and data mining and training of artificial intelligence technologies or similar technologies.
© 2026 Wiley-VCH GmbH

Among visible-light-responsive catalysts, polymer phenylethynylcopper (PECu) stands out due to its exceptionally low CB potential of −2.19 V versus the normal hydrogen electrode (NHE), demonstrating an outstanding thermodynamic capacity to efficiently drive the $O_2/O_2^{\bullet-}$ redox couple [9, 10]. This unique property makes PECu an excellent candidate for probing the ultimate limits of photocatalytic oxygen reduction. Nevertheless, the intrinsic charge excitation mode of PECu results in incomplete separation of electron–hole pairs within the C—C≡Cu unit, thereby restricting the effective utilization of photogenerated electrons and impeding the full expression of its substantial reduction potential [9, 11]. This limitation underscores the urgency of precisely tuning its electronic structure; overcoming this bottleneck could enable a remarkable enhancement in oxygen reduction performance on this inherently high-energy platform.

In regulating electronic structures, the coordinated tuning of the metal-centered d-bands and nonmetal p-bands to optimize the adsorption–desorption behavior of reaction intermediates has emerged as a new paradigm for improving catalytic performance [12, 13]. This concept of "orbital engineering" provides valuable inspiration: Can a heteroelement with an appropriately positioned p-orbital energy level be introduced to bridge the orbital energy gap between Cu 3d and C 2p in PECu? Guided by this rationale, heteroatomic chlorine (Cl) was selected as an effective regulator. Its low-energy p orbitals and moderate electronegativity enable hybridization with the Cu d orbitals and the acetylene C p orbitals, thereby improving the proximity of the d/p-band centers and reshaping the oxygen reduction pathway [11, 14].

Although the prospects are promising, a substantial research gap remains regarding the coordinated regulation of d/p orbitals through heteroatomic doping in this unique system. Specifically: (i) Driving mechanism of interfacial electronic engineering: How does Cl doping quantitatively alter the local coordination environment and the macroscopic charge transfer pathway, such as metal–metal charge transfer (MMCT), in PECu? (ii) Precise control of orbital energy levels: Can this strategy effectively narrow the energy difference between the d/p-band centers, thereby optimizing O_2 adsorption and activation? (iii) Selective guidance of reaction pathways: Can orbital engineering regulate not only the efficiency of oxygen activation but also its reaction pathway selectivity, thereby preferentially driving the single-electron reduction of $O_2^{\bullet-}$?

In this work, a highly reactive PECu platform was employed, and its electronic structure was precisely modulated through the strategic incorporation of chlorine dopants. The Cl modification was systematically elucidated to enhance metal–metal charge transfer and narrow the energy gap between the d- and p-band centers, functioning as a molecular-level "precise switch" that preferentially drives the single-electron reduction of O_2 molecules, thereby enabling the efficient and selective generation of $O_2^{\bullet-}$. Rather than simply optimizing catalytic activity through conventional band-center engineering, this work establishes orbital fine-tuning as a strategy for governing oxygen-activation pathway selectivity. By correlating d/p-band center proximity ($\Delta\varepsilon_{d\text{-}p}$) with MMCT-mediated electron-transfer behavior and $O_2^{\bullet-}$ generation, we identify $\Delta\varepsilon_{d\text{-}p}$ as a pathway-selectivity descriptor rather than a conventional activity descriptor, providing a new mechanistic framework for orbital engineering in photocatalysis.

2 | Results and Discussion

Microstructural and crystallographic analyses were conducted to verify that the colloidal-crystal templating strategy successfully enabled the selective incorporation of heteroatomic Cl into PECu. The diffraction peaks of PCC were well fitted by Rietveld refinement of the x-ray diffraction (XRD) data (Figure 1a), showing excellent agreement with the simulated crystal structure (R_{wp} = 8.60%) and confirming the $P2_1$ space group. In contrast, the XRD pattern of PECu (Figure S2) shows low crystallinity, which may originate from the weak coordination polarization field between Cu^+ and the C≡C group [15]. Remarkably, the introduction of Cl^- promoted the preferential growth of PCC along the (100) and (200) planes, a behavior attributed to the pronounced effect of d–p orbital hybridization that stabilizes the crystal structure [16, 17]. In addition, the observed lattice contraction in PCC may induce a redistribution of d–p orbital electrons and shift the d-band center downward, thereby enhancing its affinity toward oxygen-active intermediates [18].

Transmission electron microscopy (TEM) images (Figure 1b) further revealed that PCC (0.5 μm in length and 60 nm in diameter) possesses a coarser morphology than PECu (1.0 μm × 30 nm, Figure S1b). Interestingly, increasing the Cl^- concentration during synthesis caused PECu to evolve into a more stubby form and progressively assemble into a distinctive "bird's nest" architecture (Figure S1c–g). This nanorod-assembled structure generates a strong interfacial electric field [19], which facilitates the migration of photogenerated charge carriers and promotes ROS formation [20]. Energy-dispersive spectroscopy (EDS) analysis (Figure S1j,k) confirmed the successful incorporation of Cl into PCC, with no detectable Na. The Cl content gradually increased from 13.64 to 14.11 wt% with increasing NaCl dosage (Table S5), confirming the successful and controllable incorporation of chlorine into the polymeric framework. Moreover, the NaCl-based templating approach created new mesopores (d = 3.69 nm) and expanded the preexisting pore network in PCC, resulting in a 69% increase in specific surface area (Figure S5 and Table S3). This substantial increase in accessible surface area enhances the density of catalytically active sites on PCC [21].

To elucidate the local structure and coordination environment of Cu species in the catalysts, synchrotron radiation-based x-ray absorption fine structure (XAFS) spectroscopy was performed. Figure 1c presents the x-ray absorption near-edge structure (XANES) spectra and their corresponding first-derivative curves. For PECu, both the XANES profile and Cu K-edge absorption energy are located between those of Cu_2O and CuO, indicating that the Cu species exist in a mixed-valence state between Cu^+ and Cu^{2+} [22]. In contrast, the absorption edge of PCC lies between those of Cu_2O and Cu foil, suggesting the presence of $Cu^{\delta+}$ species ($0 < \delta < 1$) [23]. Such partially positively charged Cu species are generally considered more favorable for O_2 activation [24].

Furthermore, the EXAFS R-space spectra and corresponding coordination number (CN) fitting results (Figures 1d and S6;

15213757, 0, Downloaded from https://onlinelibrary.wiley.com/doi/10.1002/ange.6084718 by Guangdong University Of Technology, Wiley Online Library on [11/10/2026]. See the Terms and Conditions (https://onlinelibrary.wiley.com/terms-and-conditions) on Wiley Online Library for rules of use; OA articles are governed by the applicable Creative Commons License

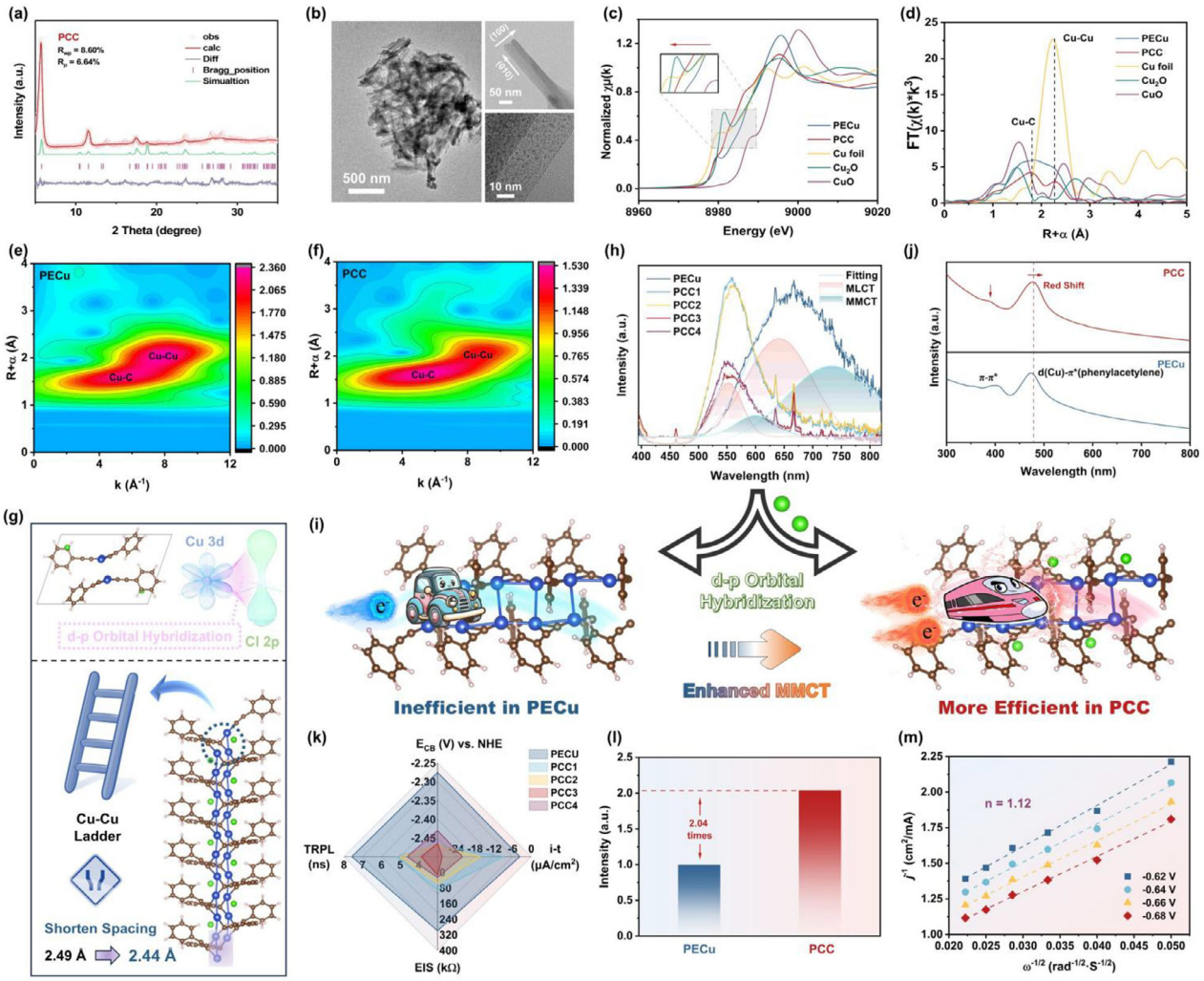


FIGURE 1 | (a) XRD Rietveld refinement result. (b) TEM image. (c) Cu K-edge XANES spectra. (d) Cu R-space Fourier-transformed k^3-weighted EXAFS spectra. WT k^3-weighted EXAFS contour plots of (e) PECu and (f) PCC. (g) Structural and d–p orbital hybridization models of PCC. (h) Steady-state PL spectra. (i) Schematic diagram of charge transfer along the Cu—Cu ladder. (j) Absorption suspension spectrum. (k) Optical and electrical properties. (l) Internal electric field strength. (m) Koutecky–Levich plots.

Table S4) reveal the coexistence of Cu—C and Cu—Cu coordination shells in both samples [25], confirming the formation of the C≡C—Cu framework. Relative to PECu, PCC exhibits a shortened Cu—Cu distance (from 2.49 to 2.44 Å), indicating enhanced electronic coupling along the Cu—Cu ladder. Simultaneously, the strengthened C≡C—Cu^+ coordination is expected to facilitate charge separation and transport. Moreover, the increased Cu—C interaction in PCC may optimize the spatial coupling between electron-transfer pathways and O_2 activation sites (Figure 1e,f), thereby promoting more efficient utilization of photogenerated electrons for O_2 activation. Figure 1g illustrates the structure and intrinsic d–p orbital hybridization of PCC, characterized by a one-dimensional Cu—Cu ladder that serves as a charge-transfer channel. Chloride doping shortens the Cu—Cu ladder spacing, while the strengthened coordination between C≡C groups and Cu^+ centers facilitates charge separation. Moreover, the enhanced orbital hybridization further optimizes the electronic structure [26].

The increased intensities of the characteristic peaks at 518 and 1927 cm^{-1}, corresponding to C—C≡C and C≡C—Cu groups, respectively, in the Fourier transform infrared (FTIR) spectra (Figure S7a) indicate an enhanced coordination interaction between C≡C and Cu^+. This interpretation is further corroborated by the x-ray photoelectron spectroscopy (XPS) analysis. The C 1s spectrum shows typical C═C/C—C/C≡C/C═O components (Figure S7b), while a slight binding-energy decrease upon Cl doping indicates increased electron density around carbon sites [27]. The Cu 2p signals remain characteristic of Cu^+ (Figure S7c), although a subtle shift to higher binding energy suggests strengthened C≡C—Cu coordination [15]. The Cl 2p spectrum (Figure S7d) and the absence of C—Cl signals in the ^{13}C nuclear magnetic resonance (NMR) spectra (Figure S9) verify that Cl is incorporated as lattice Cl^- rather than forming covalent C—Cl bonds.

Chloride incorporation markedly modulates the electronic structure of PECu. Although PCC retains nearly identical optical absorption to PECu (absorption band edge around 525 nm, Figure S10a), Cl doping induces a substantial upward shift of the CB, reaching approximately −2.465 V (Figure S10b). This more negative CB potential strongly enhances the reducing ability of photogenerated electrons, while the accompanying adjustment of

15213757, 0, Downloaded from https://onlinelibrary.wiley.com/doi/10.1002/ange.6084718 by Guangdong University Of Technology, Wiley Online Library on [11/10/2026]. See the Terms and Conditions (https://onlinelibrary.wiley.com/terms-and-conditions) on Wiley Online Library for rules of use; OA articles are governed by the applicable Creative Commons License

the valence band (VB) position reflects the d–p orbital hybridization introduced by Cl. These electronic-structure refinements, rather than changes in light-harvesting capability, are primarily responsible for the superior photocatalytic performance of PCC.

With increasing Cl^- doping, the photoluminescence (PL) intensity of PCC was suppressed (Figure 1h), with PCC3 demonstrating the most substantial quenching phenomenon [28]. This indicated that the formation of a smoother charge channel effectively separated photogenerated electron–hole pairs, a process also attributed to the enhanced internal electric field resulting from the introduction of the heteroatomic Cl [29]. Efficient charge transport performance plays a crucial role in bridging the rapid light absorption process and the slower surface reaction process. Therefore, it can be inferred that PCC3 exhibits the optimal catalytic activity [30]. Additionally, a blue shift was observed in the PL spectra of PCC, attributed to the dynamic filling of free carrier densities of states. Fitting Gaussian peaks reflected the contributions of metal-to-ligand charge transfer (MLCT) and MMCT in the charge transfer mode and photocarrier recombination [31]. Compared to PECu, the extent of MMCT recombination in PCC3 was significantly inhibited, suggesting better transfer and separation of photogenerated charges within the Cu—Cu ladder. The broadened emission peak of MMCT in PCC3 was caused by impurity levels. The contribution of MMCT in PCC3 reached 71.60% (Table S7), which disrupted the previously balanced contribution ratio between MMCT and MLCT observed in PECu. This enhanced charge transfer mode, which proceeds along the Cu–Cu ladder, improved overall charge transport performance and was more favorable for promoting photocatalytic O_2 activation (Figure 1i).

The suspension absorption spectrum of PECu and PCC (Figure 1j) revealed the electron transition modes of π–π^* and d–π^* [15]. A red shift of the d–π^* transition in PCC, compared to PECu, might result from the expansion of the material's overall coordination [15]. Additionally, the enhancement of the d–π^* transition and the decrease in the π–π^* transition indicated that the introduction of Cl^- optimized the electronic structure of PCC. This adjusted electronic transition mode was more favorable for charge transport along the Cu—Cu ladder and thereby improved photocatalytic performance.

Cl^- dopants influenced the energy level structure of PECu, leading to changes in the charge transfer mode and effectively improving the separation of photogenerated carriers. Photoelectrochemical measurements further confirm that Cl doping markedly enhances charge separation and transfer in PCC. In a radar chart of key photoelectric properties (Figure 1k), PCC (particularly PCC3) exhibits the smallest area compared to PECu, indicating substantially higher photocurrent density, lower charge-transfer resistance, and shorter carrier lifetimes (Figure S12). These characteristics collectively suggest more efficient electron extraction and faster interfacial transport within the Cu—Cu ladder structure. The results demonstrate that Cl-induced modulation of the energy levels strengthens the internal electric field and directs photogenerated electrons toward reduction-active sites rather than recombination [32]. PCC exhibited a significantly stronger internal electric field, 2.04 times greater than that of PECu (Figure 1l). This enhanced field was a key factor driving the improved kinetics of charge transfer and separation [33]. Furthermore, the stronger internal electric field facilitated the direct activation of molecular O_2 via electron transfer [34]. To further elucidate the electron transfer process, the molecular O_2 reduction pathway in PCC was investigated using a rotating disk electrode (RDE) (Figure S13). As shown in (Figure 1m), the average electron transfer number (n) for PCC, calculated from the Kocutecký–Levich (K–L) equation, was determined to be 1.12. This value indicated that molecular O_2 predominantly undergoes a single-electron reduction on PCC to generate $O_2^{\bullet-}$, a mechanism facilitated by the PCC's highly negative CB potential.

The superior electronic structure and charge transport properties of PCC suggested high efficacy for photocatalytic oxygen activation. Density functional theory (DFT) calculations reveal that O_2 does not bind stably to Cu sites but preferentially adsorbs on alkynyl units (C13 & C15) within the Cu—Cu ladder, where it readily accepts electrons to form $O_2^{\bullet-}$ (Figure 2a). Notably, the adsorption energies (E_{ads}) of O_2 on PECu and PCC were −0.797 and −1.314 eV, respectively, indicating that PCC could more readily adsorb and activate O_2 compared to PECu (Table S9). Charge-density-difference analysis (Figure 2b) further confirms enhanced and more homogeneous electron transfer to O_2 in PCC (0.975 e; 0.507 e + 0.468 e) [35], consistent with the single-electron transfer pathway identified from K–L analysis.

Enhancing the proximity of the d/p-band centers facilitated a balanced adsorption and desorption of intermediates, which was more conducive to the catalytic process [36]. To elucidate the origin of this behavior, projected density-of-states (PDOS) calculations were performed. As illustrated in Figure 2c,d, Cl doping shifts the C-p band center upward ($\varepsilon_{C\text{-}p}$, −2.093 → −1.937 eV) and the Cu-d band center downward ($\varepsilon_{Cu\text{-}d}$, −1.418 → −1.486 eV), significantly narrowing the d/p-band-center gap ($\Delta\varepsilon_{d\text{-}p}$, 0.675 → 0.339 eV). This convergence promotes a more balanced adsorption of O_2 intermediates, thereby facilitating their activation [37]. The upward shift of the C-p states near the adsorption sites further enhances O_2 binding on the alkynyl groups (Figure 2e,f), confirming that charge redistribution induced by Cl effectively tailors the surface electronic structure [38]. Notably, comparative theoretical analyses of PCC before and after Cl^- removal, including adsorption-energy calculations, crystal orbital Hamilton population (COHP) analysis (Figure S15), and bond-length evaluation, reveal that Cl^- does not directly participate in O_2 adsorption. Instead, Cl^- indirectly regulates the adsorption strength of O_2 by modulating the electronic structure of the catalyst framework, thereby influencing O_2 activation. Consistent with this interpretation, O_2 adsorption–desorption profiles support this trend, demonstrating more favorable and better-balanced O_2 binding on PCC (Figure S16). Overall, the reduced d/p-band-center separation enables optimized O_2 activation and underpins the superior photocatalytic performance of PCC.

To further verify the role of PCC in molecular O_2 activation, in situ FTIR spectra were collected under light and oxygen. As shown in Figure 3a, after oxygen adsorption, the intensity of the characteristic band located at 2270–2000 cm^{-1} increased. This band was attributed to the stretching vibration of the C≡C group on the PCC surface [39], indicating that adsorbed oxygen ($*O_2$) bound to these C≡C sites—a finding consistent

15213757, 0, Downloaded from https://onlinelibrary.wiley.com/doi/10.1002/ange.6084718 by Guangdong University Of Technology, Wiley Online Library on [11/10/2026]. See the Terms and Conditions (https://onlinelibrary.wiley.com/terms-and-conditions) on Wiley Online Library for rules of use; OA articles are governed by the applicable Creative Commons License

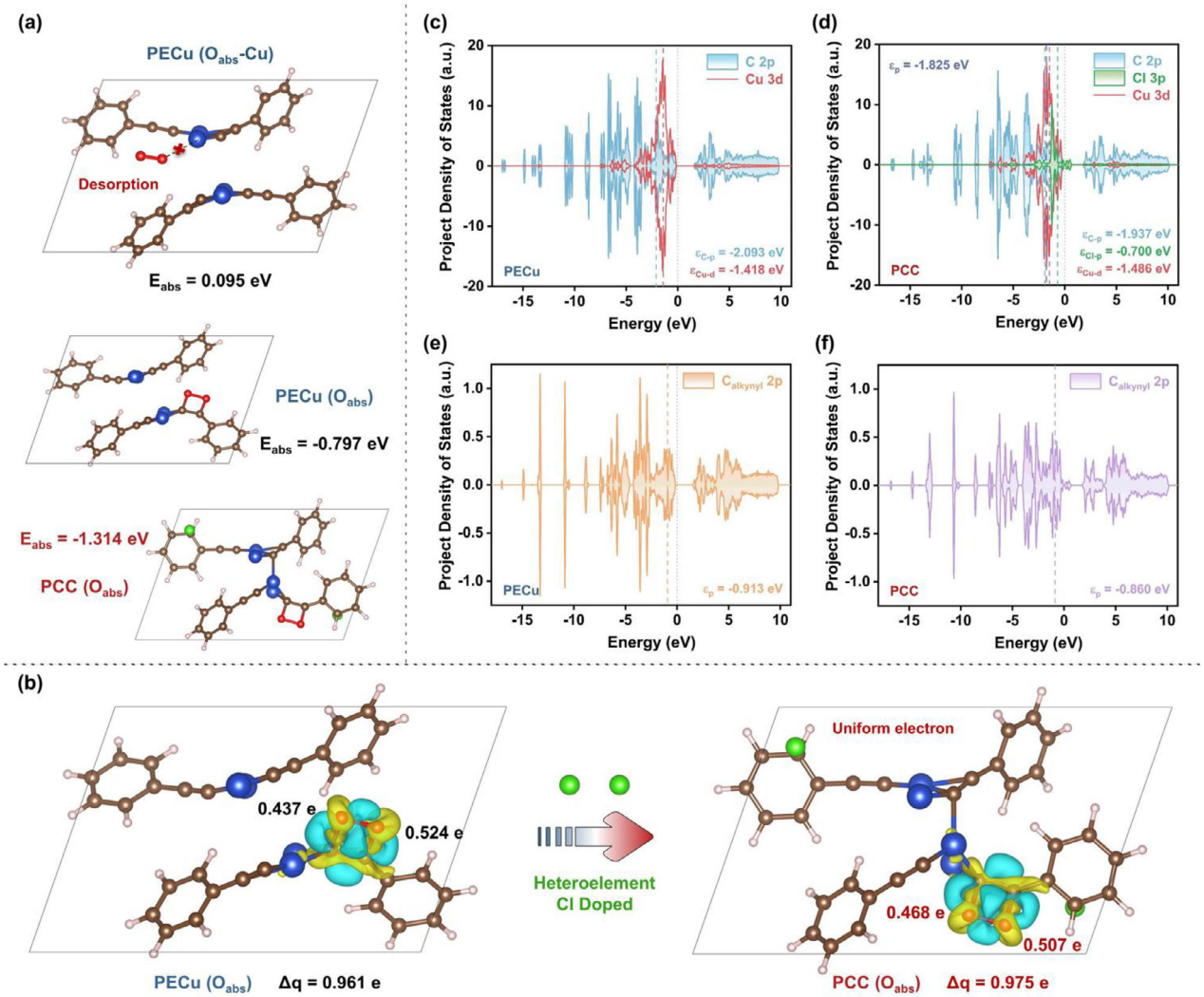


FIGURE 2 | (a) The adsorption energies of O_2 on the surface of PECu and PCC. (b) The electron transfer models of PECu and PCC systems. PDOS of (c) PECu and (d) PCC. PDOS of alkynyl group (C13 & C15) in (e) PECu and (f) PCC.

with the DFT calculation results. Notably, under light irradiation, the characteristic vibration of the C≡C-*O_2 adduct intensified. Concurrently, the vibrations of the bands representing 1411 cm^{-1} for *O_2^-, 1199 cm^{-1} for $O_2^{\bullet-}$, and 950 cm^{-1} for molecules O_2 (O—O) were gradually enhanced [40], indicating the successful activation of adsorbed O_2 and the sustained generation of ROS. The discovery of the endoperoxide intermediates suggested that the appropriate oxygen adsorption of PCC facilitated the partial retention of the O—O bond to generate $O_2^{\bullet-}$, as well as its partial cleavage to yield •OH [40, 41]. The above experimental results demonstrated that the C≡C group served as the primary active site for molecular O_2 activation, facilitating the single-electron reduction of O_2 to generate $O_2^{\bullet-}$.

Electron spin resonance (ESR) spectroscopy independently confirmed the formation of e^-, $O_2^{\bullet-}$, •OH, and $^1O_2$ (Figures 3b,c and S17). Notably, the $O_2^{\bullet-}$ signal intensity on PCC was enhanced by 3.44-fold compared to PECu, demonstrating a superior photoactivation capability. Given that •OH and $^1O_2$ serve as downstream derivatives of $O_2^{\bullet-}$ in this system, the disproportionately higher $O_2^{\bullet-}$ yield suggests it acts as the primary precursor for the entire ROS pool. Moreover, Cl^--containing PCC exhibited a positive Zeta potential (Figure 3d), with PCC3 reaching +10.51 mV, which promotes the adsorption of negatively charged $O_2^{\bullet-}$ and further enhances surface reaction kinetics.

Femtosecond transient absorption spectroscopy (fs-TAS) was employed to probe the excited-state dynamics of PECu and PCC. The results indicate that PCC exhibits more efficient photogenerated charge separation than PECu, thereby suppressing radiative recombination. As shown in Figure 3e,f, both samples display a pronounced ground state bleach (GSB) signal centered at approximately 480 nm. In contrast, PECu exhibits a distinct stimulated emission (SE) signal, whereas no detectable SE signal is observed for PCC following Cl^- incorporation. Meanwhile, the GSB intensity is significantly enhanced in PCC, suggesting more efficient exciton dissociation and charge-carrier generation (Figure 3g) [42].

Transient kinetic traces monitored at 480 nm were fitted using a biexponential decay model, yielding two characteristic lifetime components for both PECu and PCC (Figure S18). The longer-lived component (306.40 ps for PECu and 284.10 ps for PCC) is assigned to band-to-band carrier recombination, whereas the

15213757, 0, Downloaded from https://onlinelibrary.wiley.com/doi/10.1002/ange.6084718 by Guangdong University Of Technology, Wiley Online Library on [11/10/2026]. See the Terms and Conditions (https://onlinelibrary.wiley.com/terms-and-conditions) on Wiley Online Library for rules of use; OA articles are governed by the applicable Creative Commons License

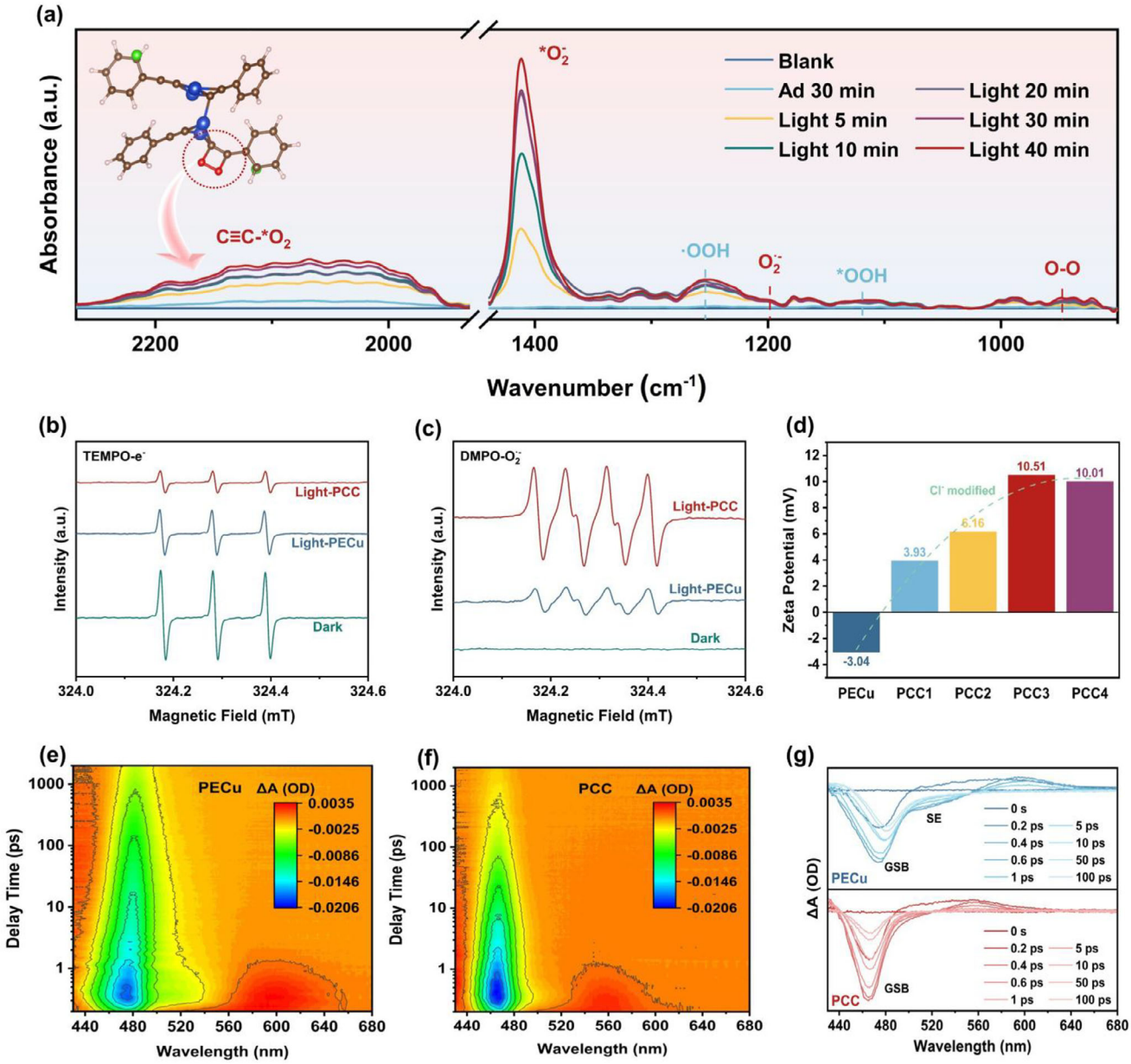


FIGURE 3 | (a) In situ FTIR spectra of PCC-induced photocatalytic oxygen activation. ESR spectra of (b) TEMPO-e$^-$ and (c) DMPO-$O_2^{\bullet-}$ in dark and light conditions. (d) Zeta potentials of PECu and PCC. Pseudo-color plots of transient absorption spectra raw data for (e) PECu and (f) PCC. (g) Femtosecond transient absorption spectra.

shorter-lived component (3.69 ps for PECu and 3.22 ps for PCC) is attributed to ultrafast charge transfer through the Cu—Cu ladder via the MMCT pathway [43]. The shortened MMCT lifetime and the disappearance of the SE signal in PCC indicate accelerated charge separation and transfer, which effectively suppresses carrier recombination and favors subsequent photocatalytic O_2 activation.

To assess the impact of heteroatomic Cl doping on O_2 activation, molecular probe experiments were carried out to quantify the generation of ROS (Figure S19). PCC exhibited a markedly higher yield of $O_2^{\bullet-}$ than PECu (Figure 4a), with PCC3 reaching 234.50 μmol/L within 20 min, which is approximately five times higher than that of PECu. Under an O_2 atmosphere with hole (h^+) scavenging, the $O_2^{\bullet-}$ yield further increased to 471.38 μmol/L (Figure 4b), highlighting the intrinsic superiority of the PCC system in single-electron O_2 activation. Owing to the enhanced proximity of the d/p-band center, the PCC series of photocatalysts demonstrated superior performance in generating $O_2^{\bullet-}$, which outperforms other recently reported photocatalysts in both the rate of $O_2^{\bullet-}$ production and the required photocatalyst mass (Figure 4c and Table S10). Furthermore, a series of Cl^- and halide-modified photocatalysts prepared using the same synthetic strategy exhibited similar enhancement trends (Figure S20), suggesting that this approach may provide a generally applicable route for regulating electronic structure and promoting photocatalytic O_2 activation.

Importantly, $O_2^{\bullet-}$ generation strongly correlated with the contribution of the MMCT pathway ($y = 8.65x - 387.73$, $R^2 = 0.9689$)

15213757, 0, Downloaded from https://onlinelibrary.wiley.com/doi/10.1002/ange.6084718 by Guangdong University Of Technology, Wiley Online Library on [11/10/2026]. See the Terms and Conditions (https://onlinelibrary.wiley.com/terms-and-conditions) on Wiley Online Library for rules of use; OA articles are governed by the applicable Creative Commons License

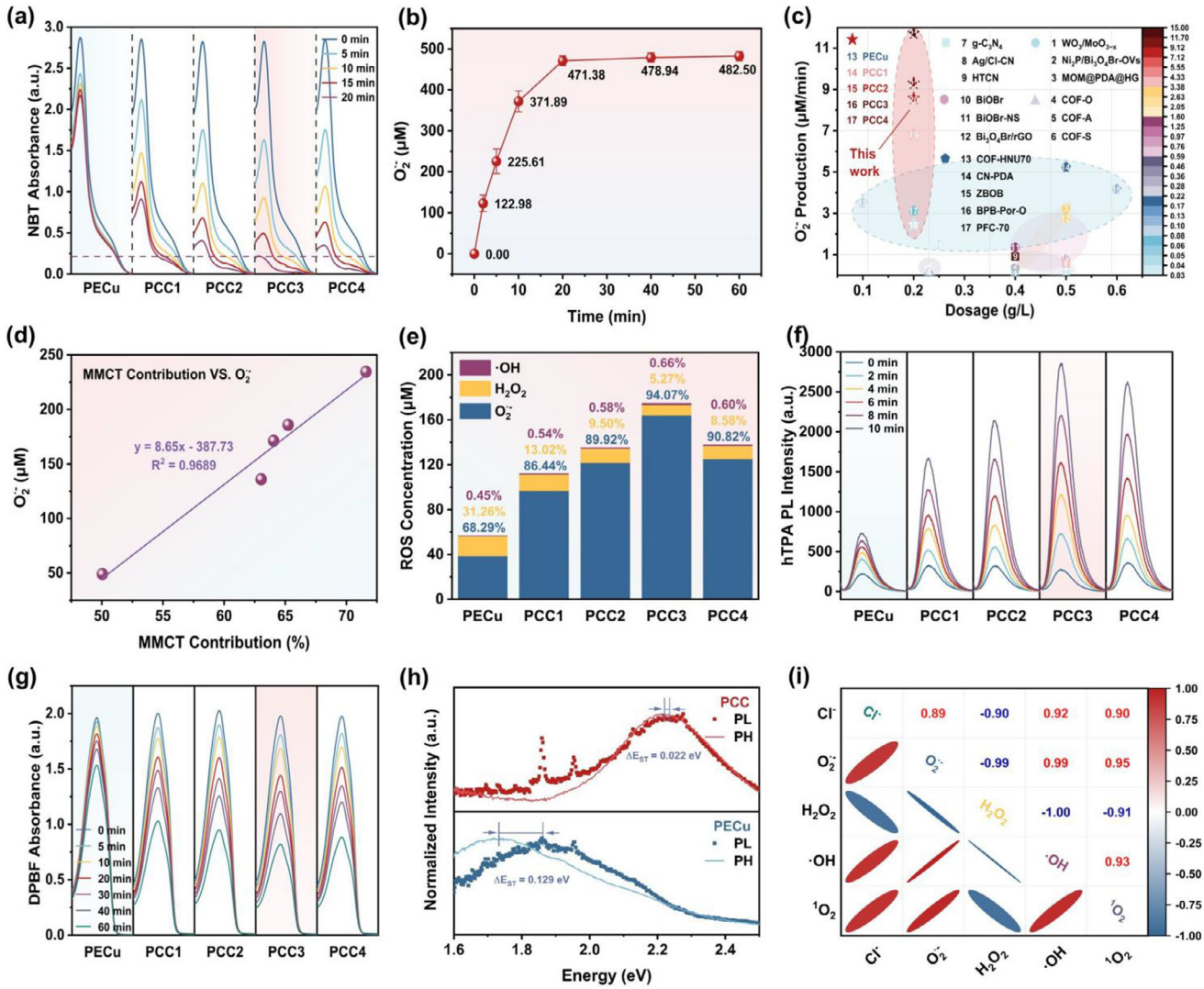


FIGURE 4 | (a) UV–vis absorbance spectra of the NBT. (b) Photocatalytic production of $O_2^{\cdot-}$ by PCC (experimental conditions: initial NBT concentration = 200 μM, initial $Na_2C_2O_4$ concentration = 10 mM, PCC dosage = 0.2 g/L, solution volume = 50 mL, O_2 atmosphere). (c) Comparison of $O_2^{\cdot-}$ production performance with recent reports. (d) The correlation between the contribution rate of MMCT and the concentration of $O_2^{\cdot-}$. (e) The proportion of $O_2^{\cdot-}$, H_2O_2, and •OH in total ROS produced at 10 min. (f) PL spectra of the hTPA. (g) UV–vis absorbance spectra of the DPBF. (h) The steady-state PL and PH spectra. (i) The correlation matrix of doped Cl^- and ROS concentration in PECu and PCC.

(Figure 4d). Although surface area and light absorption capability are commonly considered important factors governing photocatalytic activity, these parameters (R^2 < 0.75) alone cannot fully explain the enhanced $O_2^{\cdot-}$ generation performance of PCC (Figure S21). A linear relationship between MMCT and $O_2^{\cdot-}$ yield reveals that precise regulation of the MMCT excitation mode enables predictable and highly selective $O_2^{\cdot-}$ production. Combined with the spectroscopic evidence chain (XAFS, fs-TAS, in situ FTIR, and ESR), these results provide further mechanistic insight into photocatalytic oxygen activation and underscore that both generation and directional utilization of photogenerated electrons are essential to the enhanced $O_2^{\cdot-}$ generation efficiency of PCC. Among the series, PCC3 showed the highest $O_2^{\cdot-}$ selectivity, significantly surpassing H_2O_2 and •OH formation (Figure 4e). Increasing the Cl content promoted the proportion of both $O_2^{\cdot-}$ and •OH while suppressing H_2O_2, indicating that Cl-induced modulation of the d/p-band proximity enables more efficient adsorption and conversion of O_2 intermediates (Equations 1–3) [44]. The more positive zeta potential of PCC3 further facilitated the enrichment of $O_2^{\cdot-}$ near the catalyst surface, accelerating interfacial redox reactions.

$$O_2 + e^- \rightarrow O2\bullet - \quad (1)$$

$$O2\bullet - + 2H^+ + e^- \rightarrow H_2O_2 \quad (2)$$

$$H_2O_2 + H^+ + e^- \rightarrow \bullet OH + H_2O \quad (3)$$

Crucially, the Cl-induced modulation of the d/p-band proximity not only facilitates this primary activation step but also promotes the subsequent conversion of $O_2^{\cdot-}$ into other ROS. PCC also showed an increased production of •OH and $^1O_2$ (Figure 4f,g). Given the disproportionate increase in the production of $O_2^{\cdot-}$ and $^1O_2$ in PCC, it could be inferred that the conversion of adsorbed O_2 to $^1O_2$ via energy transfer was also a pathway for O_2 activation [45].

15213757, 0, Downloaded from https://onlinelibrary.wiley.com/doi/10.1002/ange.6084718 by Guangdong University Of Technology, Wiley Online Library on [11/10/2026]. See the Terms and Conditions (https://onlinelibrary.wiley.com/terms-and-conditions) on Wiley Online Library for rules of use; OA articles are governed by the applicable Creative Commons License

PL and phosphorescence (PH) analyses (Figure 4h)indicated that the energy gap (ΔE_{ST}) of PCC (0.022 eV) is significantly lower than that of PECu (0.129 eV), due to Cl-induced enhancement of spin–orbit coupling, confirmed by the reduced exciton lifetime (Figure S22), which accelerates intersystem crossing and promotes $^1O_2$ formation [46].

The intrinsic linkage between these species is further confirmed by $O_2^{\bullet-}$ quenching experiments (Figure S23), which show a concomitant decrease in •OH and $^1O_2$ concentrations, verifying that the boosted generation of all ROS is mainly driven by the enhanced $O_2^{\bullet-}$ production. Further, correlation analysis (Figure 4i) demonstrates a strong positive relationship between Cl content and the generation of $O_2^{\bullet-}$, •OH, and $^1O_2$. Collectively, these results demonstrate that Cl doping precisely modulates the electronic structure and d/p-band proximity of PCC, enabling more efficient adsorption, activation, and selective conversion of molecular oxygen, ultimately leading to a robust ROS generation system dominated by $O_2^{\bullet-}$.

The photocatalytic water decontamination performances of PCC were investigated using Cr(VI) and TCH as model contaminants. As illustrated in Figure S24, PCC3 exhibited the highest activity, achieving 99.81% Cr(VI) reduction and 89.90% TCH degradation within 10 min. The corresponding rate constants for Cr(VI) reduction (0.3778 min^{-1}) and TCH oxidation (0.2646 min^{-1}) were the highest among the series, representing 2.75- and 3.34-fold enhancements relative to PECu (Figure 5a). Additionally, the PCC photocatalysts demonstrated broad applicability toward a range of emerging contaminants (Figure 5b).

The contributions of ROS were further explored in the photocatalytic process. As displayed in Figure 5c, both Cr(VI) reduction and TCH degradation displayed strong oxygen dependence, confirming that water decontamination is dominated by O_2-derived ROS generated through molecular oxygen activation. Benefiting from the improved electronic structure and oxygen activation pathway, PCC exhibited markedly superior oxidative and reductive capacity, outperforming conventional and state-of-the-art photocatalysts (Figure 5d,e). Scavenger experiments (Figure S25) revealed that Cr(VI) photoreduction was dominated by photogenerated electrons and $O_2^{\bullet-}$, with minor contributions from •OH and h^+. For TCH degradation, $O_2^{\bullet-}$ and $^1O_2$ were identified as the primary reactive species, followed by h^+ and •OH. Notably, the concurrent high contributions of $O_2^{\bullet-}$ and $^1O_2$ indicate that $^1O_2$ is generated via $O_2^{\bullet-}$ oxidation, reaffirming the central role of $O_2^{\bullet-}$ in PCC-mediated molecular oxygen activation.

Adsorption analysis (Figures 5f and S26) revealed that PCC exhibits stronger physisorption toward Cr(VI) and chemisorption toward TCH than PECu, providing more accessible reaction sites for ROS attack [47]. These results confirm that the enhanced d/p-band modulation in PCC not only promotes O_2 activation but also strengthens pollutant–catalyst interactions, jointly contributing to its superior removal efficiency.

Establishing a quantitative structure–performance model for PCC not only clarifies the origin of its superior catalytic activity but also provides a theoretical basis for the rational design of advanced PECu-based photocatalysts. In this study, the photocatalytic performance of PCC in water purification was correlated with several key physicochemical parameters, including the XRD intensity ratio of its dominant crystal planes, specific surface area, charge-transfer excitation mode, and average fluorescence lifetime (Figure 5g). The corresponding fitting models are summarized in Table S18.

Notably, the removal efficiencies of Cr(VI) and TCH showed much stronger correlations with the intrinsic charge-transport characteristics of PCC, namely the charge-transfer excitation mode and average fluorescence lifetime ($0.8812 < R^2 < 0.9966$), than with its specific surface area ($0.6048 < R^2 < 0.7749$). The DFT-derived $\Delta\varepsilon_{d\text{-}p}$ analysis has provided an electronic origin for this enhanced charge transfer behavior. Specifically, Cl incorporation reduces the energy mismatch between Cu 3d and C 2p states, facilitating orbital hybridization and strengthening the Cu—Cu ladder-mediated charge-transfer pathway. Crucially, the surface-area-normalized rate constant (k_n) reveals a distinct lack of linearity between geometric availability and catalytic output (Figure S27). PCC3, despite not possessing the highest surface area, consistently outperformed in photocatalytic activity. This phenomenon effectively highlights d/p-band center (electronic structure) modulation as the primary descriptor, identifying surface area merely as a secondary, non-limiting factor in governing the photocatalytic activity of PCC.

Interestingly, PCC exhibited distinct correlation patterns for its crystallographic features: the reduction of Cr(VI) showed a moderate correlation with the crystal-plane intensity ratio ($R^2 = 0.7603$), whereas TCH degradation demonstrated an almost perfect correlation ($R^2 = 0.9999$). This divergence likely originates from their different removal mechanisms. Cr(VI) reduction proceeds predominantly through direct electron transfer, with $O_2^{\bullet-}$ providing secondary contributions, while TCH degradation is mainly driven by ROS. These findings further validate the scientific rationale of this work: introducing heteroatomic Cl enhances molecular oxygen activation via d–p orbital hybridization and modulates the relative positions of the d/p-band centers, ultimately optimizing the charge-transfer dynamics of PCC (Figure 5h).

The synchronous reduction of Cr(VI) and degradation of TCH generated a pronounced synergistic effect (Figure S28). Compared with the corresponding single-contaminant systems, the reaction efficiency increased by 1.85–2.60 times (Figure 6a), demonstrating the strong synergistic interaction between the reduction and oxidation processes. In the kinetic radar plot (Figure 6b) of key water purification indicators (such as total organic carbon (TOC) and total nitrogen (TN)), the area corresponding to the coexisting system is nearly 6 times larger than that of the single-pollutant systems, highlighting the remarkable capability of PCC to address complex contamination scenarios. This advantage is attributed to its optimized electronic structure and robust redox properties. Interestingly, 3D excitation–emission matrix (3DEEM) analysis showed that fewer by-products were formed during TCH degradation in the presence of Cr(VI) (Figure 6c), suggesting a more efficient TCH degradation pathway in the PCC system under coexisting conditions.

The degradation pathways and mineralization of TCH were systematically investigated (Figures 6d and S31–S33). DFT

15213757, 0, Downloaded from https://onlinelibrary.wiley.com/doi/10.1002/ange.6084718 by Guangdong University Of Technology, Wiley Online Library on [11/10/2026]. See the Terms and Conditions (https://onlinelibrary.wiley.com/terms-and-conditions) on Wiley Online Library for rules of use; OA articles are governed by the applicable Creative Commons License

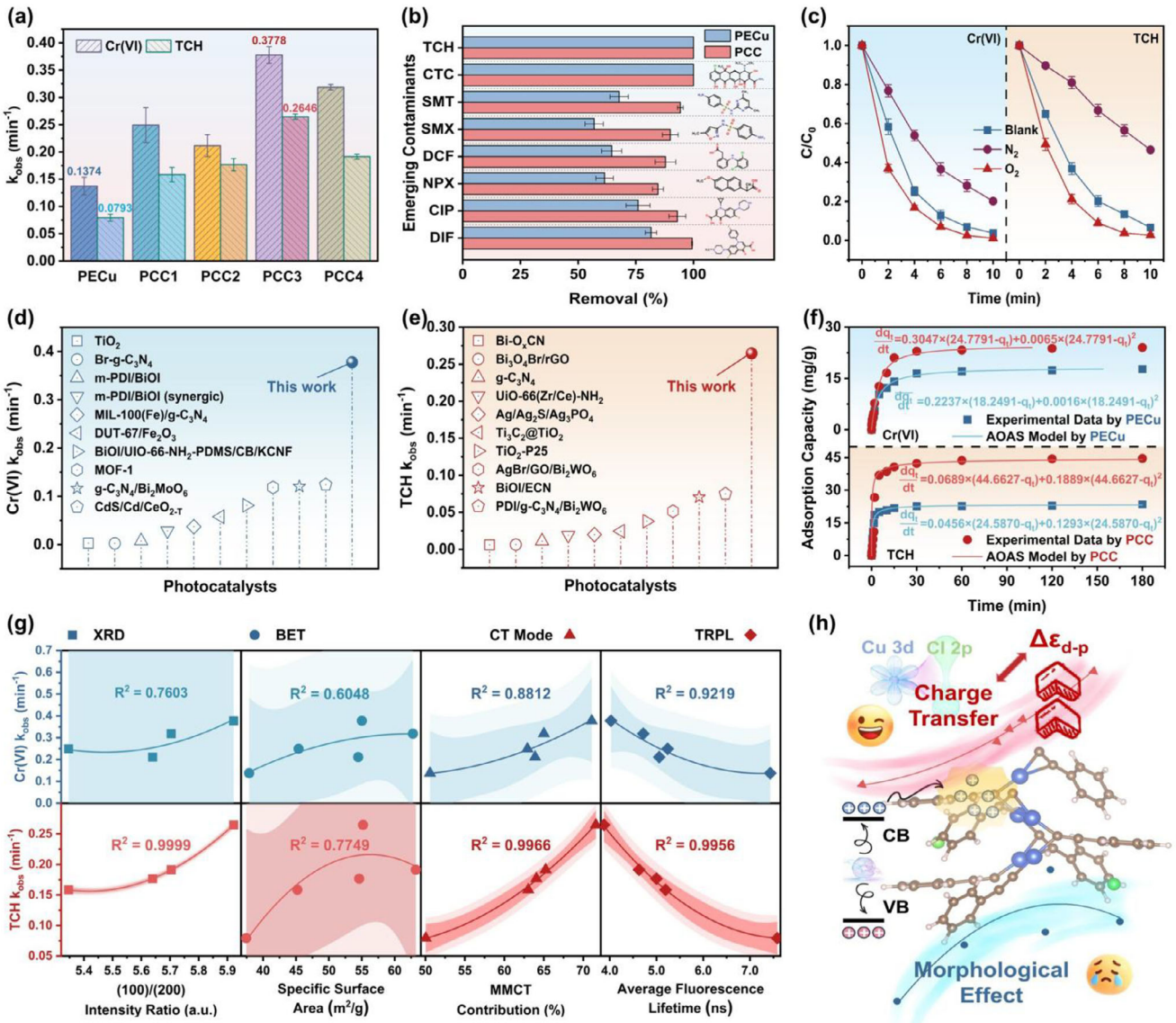


FIGURE 5 | (a) The kinetic rate constant of photocatalytic water decontamination. (b) The removal effect of emerging contaminants. (c) The photocatalytic water decontamination under different atmospheres. Comparison of reported photocatalysts on the photocatalytic degradation of (d) Cr(VI) and (e) TCH. (f) AOAS models. (g) The correlation between the kinetic rate constant of Cr(VI)/TCH and the structural properties of the PCC. (h) Schematic illustration of the optimized structure–activity relationship and charge transfer pathway in PCC.

calculations identified the C14-C16 and O21 sites as the most nucleophilic regions of TCH, rendering them highly susceptible to electrophilic attack (Figures S29 and S30). The primary degradation mechanism is initiated by the targeted attack of these surface-enriched $O_2^{\bullet-}$ species on the nucleophilic sites of TCH.

Based on intermediates identified via UPLC-Q-TOF/MS, the degradation pathways (Figure 6d) reveal that while single-TCH systems undergo a sequential process of demethylation, ring-opening, and carbonylation, the coexisting Cr(VI)/TCH system exhibits significantly accelerated kinetics and fewer intermediate accumulations. This indicates that the synergistic coupling of Cr(VI) reduction not only alleviates the recombination of photogenerated carriers but also creates an optimized reaction environment that accelerates the $O_2^{\bullet-}$-mediated decomposition of TCH. Ultimately, this leads to the deep mineralization of TCH into CO_2, H_2O, and inorganic nitrogen species (NO_3^-, NH_4^+, and N_2), confirming that the PCC system's superior capability for $O_2^{\bullet-}$ generation is the fundamental driver for both enhanced pollutant removal and mineralization.

A potential mechanism by which PCC enhances photocatalytic oxygen activation and promotes water decontamination, derived from its structure–performance relationship, is illustrated in Figure 6e. To evaluate its practical suitability, the PCC system was tested in various real-water matrices (detailed in Table S19), including electroplating wastewater, tap water, river water, seawater, and secondary effluent. Owing to its outstanding catalytic properties, PCC maintained high pollutant-removal efficiencies in all tested environments (Figure S34).

Furthermore, a small-scale reactor packed with PCC was constructed to demonstrate solar-driven water purification (Figure 6f,g). Under natural sunlight (solar spectrum and

15213757, 0, Downloaded from https://onlinelibrary.wiley.com/doi/10.1002/ange.6084718 by Guangdong University Of Technology, Wiley Online Library on [11/10/2026]. See the Terms and Conditions (https://onlinelibrary.wiley.com/terms-and-conditions) on Wiley Online Library for rules of use; OA articles are governed by the applicable Creative Commons License

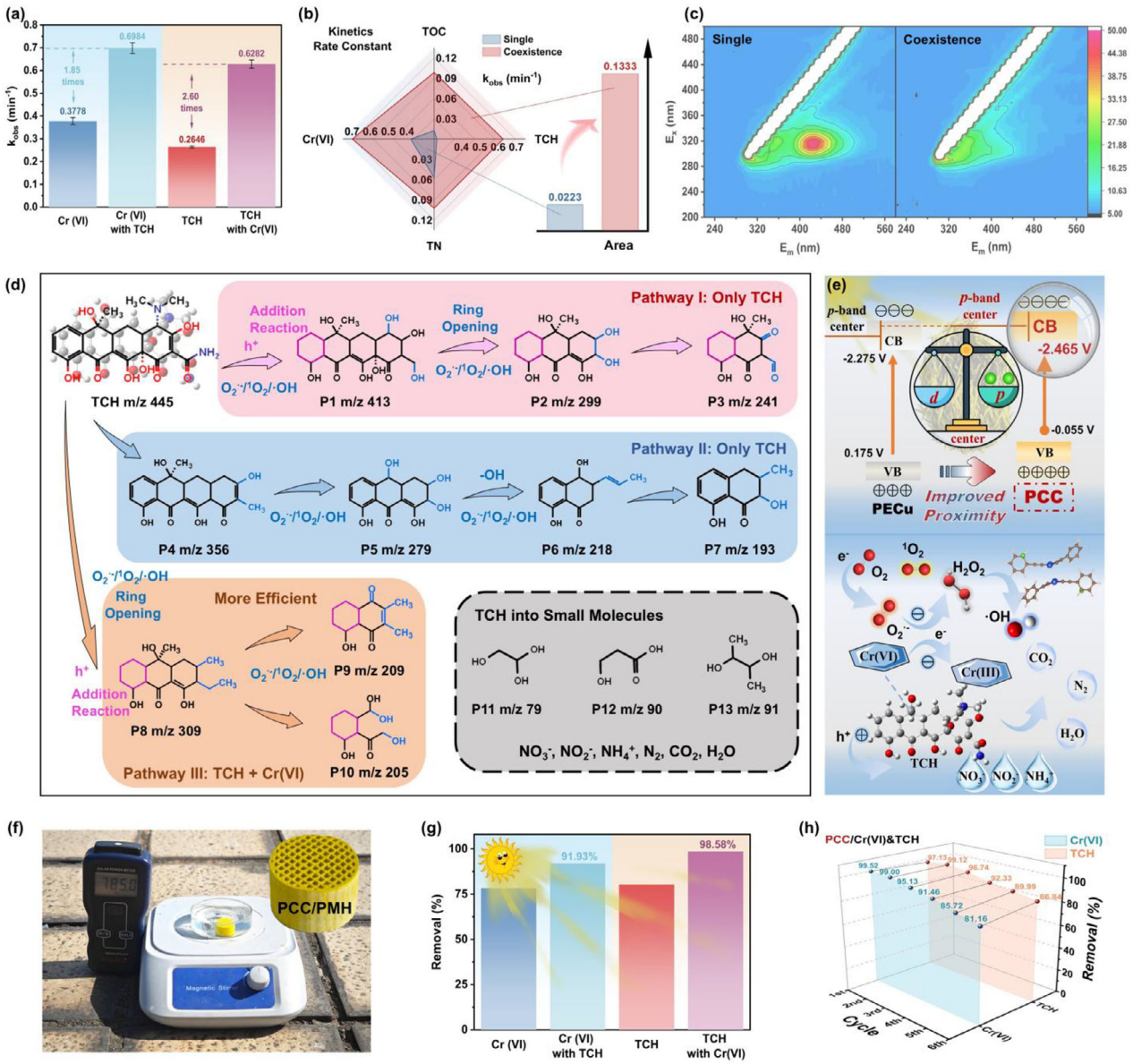


FIGURE 6 | (a) The kinetic rate constant for simultaneous contaminant removal by PCC. (b) Kinetic radar plot of the PCC system. (c) 3DEEM images during the TCH degradation. (d) Possible photodegradation pathway of TCH in PCC system. (e) Schematic representation of the photocatalytic mechanism of PCC. (f) Simple solar water treatment device (inset: digital photograph of porous mullite honeycomb loaded with PCC photocatalyst). (g) Photocatalytic water decontamination of formed catalysts under sunlight. (h) Photocatalytic water decontamination with the PCC in cycling runs.

irradiance shown in Figure S35), the system achieved removal efficiencies of 91.93% for Cr(VI) and 98.58% for TCH. As presented in Figure 6h, the PCC system sustained robust pollutant removal (> 80%) after ten consecutive cycles. The negligible changes in morphology and crystal structure after repeated use (Figure S36) further confirmed its excellent photostability.

Collectively, these results demonstrate that the PCC-based photocatalytic system provides an efficient, stable, and sustainable water treatment strategy with strong real-world application potential. Moreover, in contrast to the high toxicity of untreated Cr(VI) and TCH solutions, the PCC-treated water enabled mung bean seeds to germinate and grow normally (Figure S37), further validating the safety and reliability of the purified water. Beyond water decontamination, the PCC system also exhibited promising performance in methane C—H bond activation (Figure S38) and antibacterial applications (Figure S39), highlighting the broad applicability of this $O_2^{\bullet-}$-mediated photocatalytic system.

3 | Conclusion

In summary, we demonstrate that chlorine incorporation serves not merely as a heteroatomic dopant but as a powerful orbital regulator that finely compresses the d/p-band centers gap of PCC, thereby reshaping its charge–excitation landscape and oxygen-activation pathway. The Cl-induced enhancement of coordination polarization, Cu—Cu ladder contraction, and metal–metal charge transfer collectively establishes a highly efficient electron-transfer network, enabling highly preferential single-electron oxygen reduction and ultra-high $O_2^{\bullet-}$ generation (471.38 μmol/L). This orbital-level manipulation rationalizes

15213757, 0, Downloaded from https://onlinelibrary.wiley.com/doi/10.1002/ange.6084718 by Guangdong University Of Technology, Wiley Online Library on [11/10/2026]. See the Terms and Conditions (https://onlinelibrary.wiley.com/terms-and-conditions) on Wiley Online Library for rules of use; OA articles are governed by the applicable Creative Commons License

the markedly improved ROS profiles and the exceptional performance of PCC in water decontamination, including the synergistic removal of composite pollutants. Beyond demonstrating an efficient photocatalyst, this work reveals that orbital engineering can regulate the pathway selectivity of molecular oxygen activation. The identified $\Delta\varepsilon_{d\text{-}p}$ descriptor bridges orbital hybridization, MMCT dynamics, and selective $O_2^{\bullet-}$ generation, extending conventional band-center engineering from activity optimization toward programmable reaction-pathway control.

Author Contributions

Zili Lin: conceptualization, methodology, data curation, investigation, validation, formal analysis, writing – original draft, writing – review and editing, project administration, and resources. **Yanli Wang:** methodology, writing – review and editing, investigation, and validation. **Zhenjun Xiao:** methodology, investigation, validation, and writing – review and editing. **Ping Chen:** investigation, methodology, validation, formal analysis, funding acquisition, and resources. **Yishun Wang:** methodology, investigation, and validation. **Lingzhi Shen:** methodology, investigation, and validation. **Zheng Hu:** methodology, investigation, and validation. **Zihong Xu:** methodology, investigation, and validation. **Siling Zhang:** methodology, investigation, and validation. **Linsheng Liu:** methodology, investigation, and validation. **Zheng Fang:** software, investigation, validation, and methodology. **Daguang Li:** software, resources, investigation, and validation. **Wenying Lv:** conceptualization, resources, supervision, project administration, writing – review and editing, validation, funding acquisition, and investigation. **Guoguang Liu:** conceptualization, resources, supervision, writing – review and editing, investigation, funding acquisition, and validation.

Acknowledgments

This work was supported by the National Natural Science Foundation, China (Grant Nos. 22176042, 21906029, and 22076029), the Natural Science Foundation of Guangdong Province, China (Grant Nos. 2024A1515011742 and 2025A1515012104), and the Guangdong Province Science and Technology Innovation Strategic Fund (Project for Cultivating College Students' Scientific Innovation) (Grant Nos. pdjh2026bc395). The authors thank Assoc. Prof. Fengliang Wang (Sun Yat-sen University) and Dr. Datong Chen (South China University of Technology) for their valuable technical assistance. The authors also acknowledge the Analysis and Test Center of Guangdong University of Technology and Shiyanjia Lab (www.shiyanjia.com) for XAFS measurements.

Conflicts of Interest

The authors declare no conflicts of interest.

Data Availability Statement

The data that support the findings of this study are available from the corresponding author upon reasonable request.

References

1. S. Guo, K. Zhao, L. Liang, et al., "Fully Conjugated Sp^2 Carbon-Linked Covalent Organic Frameworks Enables Accelerated Exciton Process for Superior Singlet Oxygen Photosynthesis for Water Remediation," *Angewandte Chemie International Edition* 64 (2025): e202509141, https://doi.org/10.1002/ange.202509141.

2. M. Urso, M. Ussia, X. Peng, C. M. Oral, and M. Pumera, "Reconfigurable Self-Assembly of Photocatalytic Magnetic Microrobots for Water Purification," *Nature Communications* 14 (2023): 6969, https://doi.org/10.1038/s41467-023-42674-9.

3. R. Xie, K. Guo, Y. Li, et al., "Harnessing Air-Water Interface to Generate Interfacial ROS for Ultrafast Environmental Remediation," *Nature Communications* 15 (2024): 8860, https://doi.org/10.1038/s41467-024-53289-z.

4. J. Ge, J. Zhao, H. Ying, et al., "Photoetching-Generated Redox Pairs in Confined Layered Structure Boost Single-Electron-Transfer-Mediated Photocatalysis," *Journal of the American Chemical Society* 147 (2025): 39732–39738, https://doi.org/10.1021/jacs.5c13187.

5. S. Cao, S. Zheng, T. Liu, et al., "Interfacial Oxygen Vacancy-Metal Dual-Sites on $NiFe_2O_4$/Ni@NC Dictating Dominant Singlet Oxygen Evolution From Peroxymonosulfate Activation," *Applied Catalysis B: Environment and Energy* 383 (2026): 126045, https://doi.org/10.1016/j.apcatb.2025.126045.

6. R. Wu, S. Gao, C. Jones, et al., "Bi/BSO Heterojunctions via Vacancy Engineering for Efficient Photocatalytic Nitrogen Fixation," *Advanced Functional Materials* 34 (2024): 2314051, https://doi.org/10.1002/adfm.202314051.

7. Y. Chen, S. Ji, W. Sun, et al., "Engineering the Atomic Interface With Single Platinum Atoms for Enhanced Photocatalytic Hydrogen Production," *Angewandte Chemie International Edition* 59 (2020): 1295–1301, https://doi.org/10.1002/ange.201912439.

8. B. Liu, X. Wang, Y. Zhang, et al., "A $BiVO_4$ Photoanode With a VO_x Layer Bearing Oxygen Vacancies Offers Improved Charge Transfer and Oxygen Evolution Kinetics in Photoelectrochemical Water Splitting," *Angewandte Chemie International Edition* 62 (2023): e202217346, https://doi.org/10.1002/ange.202217346.

9. H.-Y. Jiang, P. Zhou, Y. Wang, et al., "Copper-Based Coordination Polymer Nanostructure for Visible Light Photocatalysis," *Advanced Materials* 28 (2016): 9776–9781, https://doi.org/10.1002/adma.201603556.

10. Z. Lin, Y. Wu, X. Jin, et al., "Facile Synthesis of Direct Z-Scheme UiO-66-NH_2/PhC_2Cu Heterojunction With Ultrahigh Redox Potential for Enhanced Photocatalytic Cr(VI) Reduction and NOR Degradation," *Journal of Hazardous Materials* 443 (2023): 130195, https://doi.org/10.1016/j.jhazmat.2022.130195.

11. Z. Wei, J. Hu, K. Zhu, W. Wei, X. Ma, and Y. Zhu, "Self-Assembled Polymer Phenylethnylcopper Nanowires for Photoelectrochemical and Photocatalytic Performance Under Visible Light," *Applied Catalysis B: Environmental* 226 (2018): 616–623, https://doi.org/10.1016/j.apcatb.2017.12.070.

12. J. Yin, J. Jin, Z. Yin, et al., "The Built-in Electric Field Across FeN/Fe_3N Interface for Efficient Electrochemical Reduction of CO_2 to CO," *Nature Communications* 14 (2023): 1724, https://doi.org/10.1038/s41467-023-37360-9.

13. F. Wu, X. Zhang, L. Wang, et al., "Enhanced Spin-Polarized Electric Field Modulating p-Band Center on Ni-Doped Cds for Boosting Photocatalytic Hydrogen Evolution," *Small* 20 (2024): 2309439.

14. S. B. Roy, S. Moon, K. Hee kim, et al., "Tuning the Band (p and d) Center and Enhancing the Active Sites by Nitrogen(N) Doping on Iridium Diphosphide (IrP2) for Accelerating pH-Universal Water Electrolysis," *Applied Catalysis B: Environmental* 319 (2022): 121906, https://doi.org/10.1016/j.apcatb.2022.121906.

15. H. Sun, Z. Zhao, Y. Xing, et al., "Charge Separation to Facilitate the Conversion of Copper-Phenylacetylide From Aggregation-Induced Emission to Efficient Photocatalysis," *Advanced Functional Materials* 34 (2024): 2311591, https://doi.org/10.1002/adfm.202311591.

16. S. S. Y. Chui, M. F. Y. Ng, and C.-M. Che, "Structure Determination of Homoleptic Au I, Ag I, and Cu I Aryl/Alkylethynyl Coordination Polymers by X-Ray Powder Diffraction," *Chemistry—A European Journal* 11 (2005): 1739–1749, https://doi.org/10.1002/chem.200400881.

17. M. Deng, M. Xia, Y. Wang, X. Ren, and S. Li, "Synergetic Catalysis of p–d Hybridized Single-Atom Catalysts: First-Principles Investigations," *Journal of Materials Chemistry A* 10 (2022): 13066–13073, https://doi.org/10.1039/D2TA03368B.

15213757, 0, Downloaded from https://onlinelibrary.wiley.com/doi/10.1002/ange.6084718 by Guangdong University Of Technology, Wiley Online Library on [11/10/2026]. See the Terms and Conditions (https://onlinelibrary.wiley.com/terms-and-conditions) on Wiley Online Library for rules of use; OA articles are governed by the applicable Creative Commons License

18. J. Li, Y. Qin, T. Tan, et al., "Enhancing the Activity of FeNi Bimetallic Electrocatalysts on Overall Water Splitting by Nd_2O_3-Induced FeNi Lattice Contraction," *Journal of Energy Chemistry* 87 (2023): 42–50, https://doi.org/10.1016/j.jechem.2023.08.021.

19. Y. Li and W. Shen, "Morphology-Dependent Nanocatalysts: Rod-Shaped Oxides," *Chemical Society Reviews* 43 (2014): 1543–1574, https://doi.org/10.1039/C3CS60296F.

20. Y. Shang, W. Li, Y. Ma, et al., "Rapid Hole Generation via D–A Structure-Dependent Built-In Electric Field of Deacetylated Chitin-PDI for Efficient Photocatalytic Oxidation," *Advanced Functional Materials* 34 (2024): 2406533, https://doi.org/10.1002/adfm.202406533.

21. Y. Liu, Y. Wang, Y. Wang, et al., "Nanochanneling and Local Crystallization Engineering Accelerate Multiphase Single-Atom Catalysis for Rapid Water Decontamination," *Angewandte Chemie International Edition* 64 (2025): e202504571, https://doi.org/10.1002/ange.202504571.

22. C. W. Li and M. W. Kanan, "CO_2 Reduction at Low Overpotential on Cu Electrodes Resulting From the Reduction of Thick Cu_2O Films," *Journal of the American Chemical Society* 134 (2012): 7231–7234, https://doi.org/10.1021/ja3010978.

23. D. Yao, Y. Wang, Y. Li, et al., "Scalable Synthesis of Cu Clusters for Remarkable Selectivity Control of Intermediates in Consecutive Hydrogenation," *Nature Communications* 14 (2023): 1123, https://doi.org/10.1038/s41467-023-36640-8.

24. H. Mistry, A. S. Varela, C. S. Bonifacio, et al., "Highly Selective Plasma-Activated Copper Catalysts for Carbon Dioxide Reduction to Ethylene," *Nature Communications* 7 (2016): 12123, https://doi.org/10.1038/ncomms12123.

25. W. Xu, W. Zhou, D. Ye, et al., "Tuning Cu–Cu Spacing in Single-Atomic Layer Cu Catalysts for Efficient and Stable CO_2-to-C_2H_4 Electroreduction," *Advanced Materials* 38 (2026): e22842, https://doi.org/10.1002/adma.202522842.

26. A. Zhu, S. Niu, N. Zhao, Z. Zhang, and W. Xie, "Modulating Copper Ladder Spacing in Copper Phenylacetylide for Enhanced Photocatalysis via Substituent Control," *ACS Applied Materials & Interfaces* 16 (2024): 50870–50878, https://doi.org/10.1021/acsami.4c11423.

27. Y. Wu, X. Liu, D. Han, et al., "Electron Density Modulation of $NiCo_2S_4$ Nanowires by Nitrogen Incorporation for Highly Efficient Hydrogen Evolution Catalysis," *Nature Communications* 9 (2018): 1425, https://doi.org/10.1038/s41467-018-03858-w.

28. X. Fan, Z. Wang, T. Lin, et al., "Coordination Chemistry Engineered Polymeric Carbon Nitride Photoanode With Ultralow Onset Potential for Water Splitting," *Angewandte Chemie International Edition* 61 (2022): e202204407, https://doi.org/10.1002/ange.202204407.

29. H. Lu, H. Yin, J. Harmer, et al., "Single-Atom Catalysts with p-Block Metals Surpass Transition-Metal Counterparts in the Photocatalytic H_2O_2 Production," *Angewandte Chemie International Edition* 64 (2024): e202413769.

30. Z. Wang and L. Wang, "Progress in Designing Effective Photoelectrodes for Solar Water Splitting," *Chinese Journal of Catalysis* 39 (2018): 369–378, https://doi.org/10.1016/S1872-2067(17)62998-X.

31. Z. Lin, Z. Xiao, Y. Liu, et al., "Insights Into Copper(I) Phenylacetylide With In-Situ Transformation of Oxygen and Enhanced Visible-Light Response for Water Decontamination: Cu–O Bond Promotes Exciton Dissociation and Charge Transfer," *Journal of Colloid and Interface Science* 671 (2024): 1–14, https://doi.org/10.1016/j.jcis.2024.05.159.

32. Y. Liu, A. Deng, Y. Yin, et al., "Modulation of Catalyst Microenvironments in $ZnIn_2S_4$/g-C_3N_4 S-Scheme Heterojunction for Ratio-Tunable Syngas Production From CO_2 Photoreduction," *Applied Catalysis B: Environment and Energy* 362 (2025): 124724, https://doi.org/10.1016/j.apcatb.2024.124724.

33. X. Xu, J. Meng, J. Huang, et al., "Ti_3C_2 Quantum Dots-Bridged $CsPbBr_3$/Faceted $Bi_2O_2CO_3$ for Efficient Photocatalytic NO/CO_2 Conversion via Internal Electric Field," *Applied Catalysis B: Environment and Energy* 379 (2025): 125725, https://doi.org/10.1016/j.apcatb.2025.125725.

34. Q. Song, Z. Li, Q. Peng, et al., "Linkage Orientation Engineering of Covalent Organic Frameworks Enables Flexible Generation of Reactive Oxygen Species in Photocatalytic O_2 Activation," *Applied Catalysis B: Environment and Energy* 378 (2025): 125619, https://doi.org/10.1016/j.apcatb.2025.125619.

35. S. Wang, E. Zhu, Y. Huang, and H. Heinz, "Direct Correlation of Oxygen Adsorption on Platinum-Electrolyte Interfaces With the Activity in the Oxygen Reduction Reaction," *Science Advances* 7 (2021): eabb1435, https://doi.org/10.1126/sciadv.abb1435.

36. Y. Liu, T. Sakthivel, F. Hu, et al., "Enhancing the d/p-Band Center Proximity With Amorphous-Crystalline Interface Coupling for Boosted pH-Robust Water Electrolysis," *Advanced Energy Materials* 13 (2023): 2203797, https://doi.org/10.1002/aenm.202203797.

37. K. Ding, Y. Yang, J. Hu, et al., "p-Block Anion Compressed d/p Band Center of Bifunctional Oxygen Electrocatalysts for Durable Aqueous Zn–Air Batteries," *Energy Storage Materials* 71 (2024): 103654, https://doi.org/10.1016/j.ensm.2024.103654.

38. Z. Liu, Y. Tian, S. Yao, Y. Li, Y. Fu, and Q. Zhou, "Interfacial Interaction-Induced Shift of d-Band Center Promotes Photocatalytic Antibiotics Mineralization," *Applied Catalysis B: Environment and Energy* 352 (2024): 123998, https://doi.org/10.1016/j.apcatb.2024.123998.

39. U. Szczepaniak, M. Turowski, T. Custer, et al., "Infrared and Raman Spectroscopy of Methylcyanodiacetylene (CH_3C_5N)," *ChemPhysChem* 17 (2016): 3047–3054, https://doi.org/10.1002/cphc.201600437.

40. Y. Zhou, Y. Wu, Z. Luo, et al., "Regulating Reactive Oxygen Species Over M–N–C Single-Atom Catalysts for Potential-Resolved Electrochemiluminescence," *Journal of the American Chemical Society* 146 (2024): 12197–12205, https://doi.org/10.1021/jacs.4c02986.

41. E. P. Delmo, Y. Wang, Y. Song, et al., "In Situ Infrared Spectroscopic Evidence of Enhanced Electrochemical CO_2 Reduction and C–C Coupling on Oxide-Derived Copper," *Journal of the American Chemical Society* 146 (2024): 1935–1945, https://doi.org/10.1021/jacs.3c08927.

42. Z. Liu, Y. Ma, J. Li, et al., "Regulating Exciton Dissociation and Photocatalytic CO_2 Reduction Over Single-Atom Cu-In_2S_3 Nanosheets," *Advanced Materials* 38 (2026): e12150, https://doi.org/10.1002/adma.202512150.

43. K. Meng, J. Zhang, B. Zhu, C. Jiang, H. García, and J. Yu, "Interfacial Charge Transfer in ZnO/COF S-Scheme Photocatalyst via Zn—N Bond," *Advanced Materials* 37 (2025): 2505088, https://doi.org/10.1002/adma.202505088.

44. Y. Wu, F. Wang, X. Jin, et al., "Highly Active Metal-Free Carbon Dots/g-C_3N_4 Hollow Porous Nanospheres for Solar-Light-Driven PPCPs Remediation: Mechanism Insights, Kinetics and Effects of Natural Water Matrices," *Water Research* 172 (2020): 115492, https://doi.org/10.1016/j.watres.2020.115492.

45. H. Wang, S. Chen, D. Yong, et al., "Giant Electron–Hole Interactions in Confined Layered Structures for Molecular Oxygen Activation," *Journal of the American Chemical Society* 139 (2017): 4737–4742, https://doi.org/10.1021/jacs.6b12273.

46. W. Liu, H. Che, B. Liu, and Y. Ao, "Unveiling the Mechanism on Photocatalytic Singlet Oxygen Generation Over Rationally Designed Carbonylated Carbon Nitride," *Journal of Materials Chemistry A* 12 (2024): 13427–13434, https://doi.org/10.1039/D4TA00835A.

47. Z. Hu, T. Wu, Z. Dong, et al., "A Novel Loofah-Like Chitosan/Alginate Composite Aerogels Prepared for Efficient Removal of Perchlorate: Experimental and DFT Study," *Chemical Engineering Journal* 491 (2024): 151969, https://doi.org/10.1016/j.cej.2024.151969.

Supporting Information

Additional supporting information can be found online in the Supporting Information section.

Supporting File: ange74381-sup-0001-SuppMat.docx.

15213757, 0, Downloaded from https://onlinelibrary.wiley.com/doi/10.1002/ange.6084718 by Guangdong University Of Technology, Wiley Online Library on [11/10/2026]. See the Terms and Conditions (https://onlinelibrary.wiley.com/terms-and-conditions) on Wiley Online Library for rules of use; OA articles are governed by the applicable Creative Commons License